JOURNAL OF PROPULSION AND POWER
Vol. 17, No. 4, July–August 2001

Blade-Row Interaction in a High-Pressure Turbine

V. S. P. Chaluvadi,* A. I. Kalfas,† M. R. Banieghbal,† H. P. Hodson,‡ and J. D. Denton‡
University of Cambridge, Cambridge, England CB3 ODY, United Kingdom

This paper presents a study of the three-dimensional flowfield within the blade rows of a single-stage high-pressure axial turbine (low-speed, large-scale). Measurements have been performed in the stationary and rotating frames of reference. Time-mean data have been obtained using five-hole pneumatic probes. The transport mechanisms of the stator wake and passage vortices through the rotor blade row have been studied using smoke flow visualization. Furthermore, unsteady measurements have been carried out using a three-axis hot wire. Steady and unsteady numerical simulations have been performed using a structured three-dimensional Navier–Stokes solver to further understand the blade-row interactions. The transport of the stator viscous flow through the rotor blade-row is described. The rotor passage vortices are affected by the transport of the stator secondary flow. It is observed that the stator secondary flow vortices are convected through the downstream rotor blade-row in a similar but not identical way to the wake. At the hub the kinematic interaction between the stator and the rotor passage vortices has two effects. First, the suction side leg of the stator passage vortex is displaced radially upwards over the developing rotor passage vortex at the hub. Additionally, the pressure side leg of the stator passage vortex is entrained into the rotor passage vortex. The predicted flowfield was interrogated from the perspective of loss production. The contribution of the unsteady flow to the stage loss has been evaluated using unsteady numerical simulations. The effect of stator viscous flow transport on the rotor flow angles is also discussed in brief. Finally, a kinematic model is proposed for the transport of the secondary-flow vortices in the downstream blade-row based on the understanding obtained from the measurements and numerical simulations.

Nomenclature

C = blade chord
H = boundary-layer shape factor (δ^*/θ)
h = blade span
h_0 = exit stagnation enthalpy
$\dot{m}$ = mass-flow rate
P_0 = stagnation pressure
p = rotor blade pitch
Re = Reynolds number
s = entropy
T = exit stagnation temperature
Tu = turbulence intensity
t = time measured from once-per-revolution trigger
V = velocity
V_{ref} = nominal stator midspan exit velocity $= V_{x1}/\cos 74$ deg
Y = stagnation pressure loss coefficient $= \Delta P_0/\frac{1}{2}\rho V_{\mathrm{ref}}^2$
y = pitchwise distance
δ^* = boundary-layer displacement thickness
ζ = vorticity
θ = boundary-layer momentum thickness
τ = blade passing period
ω = entropy flux

Subscripts

aru = additional random unsteadiness
min = minimum
r = radial
rms = root mean square
s = steady
u = unsteady
x = axial
θ = tangential

I. Introduction

THE need for a better understanding of unsteady effects on the aerodynamics, heat transfer, and noise in turbomachinery is increasing as the demand for higher gas turbine efficiency rises. The most significant contribution to the unsteadiness in a turbine is caused by the periodic chopping of the wake[1] and secondary-flow vortices from the upstream blade row by the downstream blade row.[2–5] As modern engine design philosophy places emphasis on higher blade loading and smaller engine length, the effects of these interactions become even more important.

For a turbine with a low aspect ratio and high blade turning angle, secondary flow interactions could become more important than those caused by wakes. It is possible for the incoming vortices to burst,[6,7] giving rise to very high levels of freestream turbulence. Sharma et al.[2,8] showed that the interaction of the first rotor secondary flows with the succeeding second stator blade-row appears to dominate the flowfield even at the exit of the second stator. In the turbine under investigation, the flow is subsonic. Thus, the primary source of unsteadiness is the interaction of the blade-row with the upstream blade wake and the secondary flow vortices. The objective of this study is to investigate the three-dimensional flowfield of a single-stage turbine. The origin, the nature, and the convection of the secondary flow vortices through the downstream blade-row have been studied. Their effect on the overall performance has been investigated.

II. Experimental and Numerical Approach

A. Test Rig and Instrumentation

The present work has been carried out in a subsonic large-scale, single-stage, axial flow high-pressure turbine with a casing diameter of 1.524 m and a hub-tip ratio of 0.8. Hodson[1] has described the test facility. Figure 1 shows the schematic diagram of the single-stage turbine test facility. The large scale of the rig makes it possible to measure the flowfield inside the blade passage, upstream and downstream of the blade rows.

Trip wires of 1.2 mm dia are used to ensure that the boundary layers at the hub ($\delta^*/h = 0.006$, $H = 1.41$) and casing ($\delta^*/h = 0.0069$, $H = 1.42$) are turbulent at the inlet to the stator row. These are located at two stator axial chords upstream of the stator blade row. Further details of the turbine are given in Table 1.

Received 18 January 2000; accepted for publication 8 December 2000.

*Research Student, Whittle Laboratory; currently Researcher, GE Aircraft, Engines, Cincinnati, OH.

†Research Associate, Whittle Laboratory.

‡Professor, Whittle Laboratory.

Table 1 Turbine geometry and test conditions

Head	Stator	Rotor
Flow coefficient V_{x1}/U_m	——	0.3
Stage loading	——	1.0
Stage reaction	——	0.5
Midspan upstream axial gap, mm	——	47.4
Hub-tip radius ratio	0.8	0.8
Number of blades	36	42
Mean radius, m	0.6858	0.6858
Rotational speed, rpm	——	550
Midspan chord, mm	150	124
Midspan pitch-chord ratio	0.8	0.83
Aspect ratio	1.01	1.22
Tip clearance, mm	——	1.4
Inlet axial velocity, m/s	11.8	——
Midspan inlet angle (from axial)	0.0 deg	4.8 deg
Midspan exit angle (from axial)	74.3 deg	−74.4 deg
Chord-based Reynolds number	4.7×10^5	3.8×10^5
Inlet freestream turbulence	0.25%	——

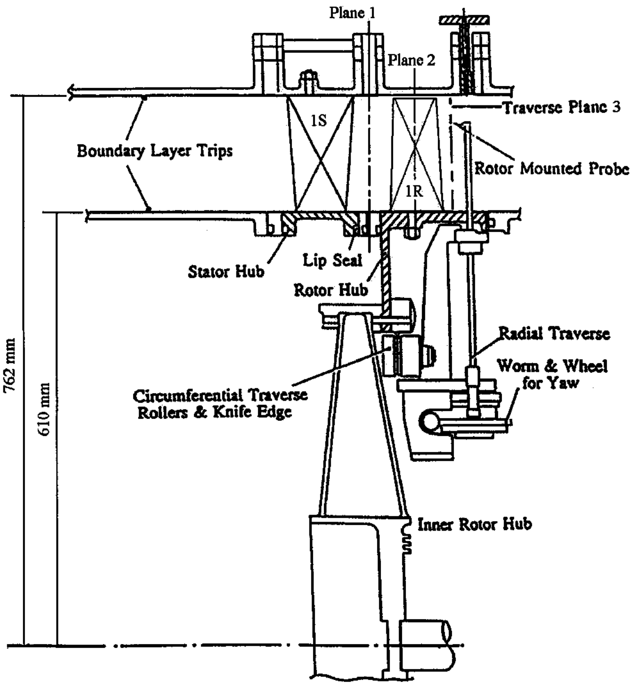

Fig. 1 Schematic of the single-stage large-scale axial flow turbine.

A Scanivalve system with integral pressure transducer is fitted to the rotor. Slip rings transfer power to and signals from the rotor mounted instruments. The rotor is designed to accommodate a three-axis relative frame traverse system in order to measure the flowfield within and at the exit of the rotor. Area traverses were carried out downstream of the blade rows and within the blade rows using a five-hole, a three-hole, or a Kiel probe. In all of the measurements, the probes were small relative to the blades, having diameters of less than 1.5% of the blade pitch. The axes of the probes were aligned parallel to the mean flow direction in order to minimize the errors. The traversing was achieved using a computer-controlled stepper motor system.

The five-hole probe was traversed radially from hub to tip in 29 steps and circumferentially over one pitch in 19 steps. The measurement grid was spaced differently such that fine resolution can be obtained in the region of large gradients of total pressure such as the blade wake and secondary flows.

B. Hot-Wire Anemometry

The development of the stator flow within the rotor blade passage was investigated using a miniature three-axis hot-wire probe. The probe had a measurement volume of 2 mm in diameter. Because of the length-diameter ratio of the hot-wire sensor ($l/d = 100$), it was not appropriate to use the "cosine law" or its modifications to represent the response of the sensors at different angles of attack.[9] For this reason a technique similar to that used for calibrating a five-hole pneumatic probe was developed. The technique relies on the interpolation of the data contained in a look-up table. Two nondimensional coefficients, derived from the apparent velocities indicated by the three sensors, were used as coordinates for the table. Each anemometer output signal was recorded at a logging frequency of 5.2 kHz using a computer controlled 12-bit transient-capture system.

All of the measured voltages were converted to velocities before the determination of the statistical quantities. The acquisition of the data was triggered using a once-per-revolution signal. For the phase-locked data measurements 48 samples were recorded in the time taken for the rotor to move past three stator pitches. The data were ensembled over 200 revolutions and about 300 points (17 points pitchwise, 19 points radially) were taken within the area traverse. The ensemble mean of N realizations of a quantity $\alpha(t, n)$ is then defined by

$$\langle\alpha(t)\rangle = \frac{1}{N}\sum_{n=1}^{N}\alpha(t, n) \tag{1}$$

where time t is measured from a once-per-cycle datum point for a periodic process. The time mean of $\alpha(t, n)$ is denoted by $\bar{\alpha}$. The ensemble rms is defined as

$$\mathrm{rms} = \sqrt{\langle\langle\alpha(t)^2\rangle\rangle} = \sqrt{\frac{1}{N}\sum_{n=1}^{N}[\alpha(t, n) - \langle\alpha(t)\rangle]^2} \tag{2}$$

It represents the amount of deviation, positive or negative, from the average value of the signal at that phase. The turbulence intensity data presented in this paper represent the mean of all of the three velocity components. This is given as

$$\langle\langle Tu_{\mathrm{rms}}\rangle\rangle = \sqrt{\tfrac{1}{3}\left(\langle\langle V_x\rangle\rangle^2 + \langle\langle V_r\rangle\rangle^2 + \langle\langle V_\theta\rangle\rangle^2\right)}\Big/ V_{\mathrm{ref}} \tag{3}$$

The time-mean rms value is determined according to

$$\sqrt{\overline{\langle\langle\alpha^2\rangle\rangle}} = \sqrt{\frac{1}{\tau}\sum_{n=1}^{\tau}\langle\langle\alpha(t)^2\rangle\rangle} \tag{4}$$

For the presentation of unsteady measurements, the time t is nondimensionalised by the wake passing period τ. The spanwise coordinate is usually expressed as a fraction of the distance from the hub to the casing.

C. Numerical Approach

The numerical simulations discussed in this paper were performed with a steady Navier–Stokes solver MULTIP81 and a time-accurate Navier–Stokes solver UNSTREST of Denton.[10–12] These codes solve the three-dimensional modified Reynolds-averaged Navier–Stokes equations on a structured, nonadaptive mesh. The equations of motion are discretized to second-order accuracy and integrated forward in time. A mixing length model with wall function is used for modeling the turbulence in the flow. For the steady-state calculations a full multigrid method and local time stepping are used to accelerate the convergence. In the case of unsteady calculations, multiple blade rows are calculated with the blade count adjusted so as to achieve an integer number of blades in each row. Fixing the ratio of the blade numbers reduces the storage requirements and computing time. Each passage is calculated in turn and the resulting primary variables stored globally. Once all of the passages have been updated, periodicity is applied along the passage boundaries. A sliding interface plane between the blade rows allows properties to pass from one blade row to another. The calculation is taken to be converged after a periodic solution is obtained in one blade passing period.

A grid of $34 \times 91 \times 45$ points for the stator and $34 \times 97 \times 45$ points for the rotor has been employed in these numerical simulations in the pitchwise, streamwise, and spanwise directions, respectively. The grid expansion ratio determines the rate at which the grid is stretched away from the solid boundaries until the maximum permitted cell size is reached. Grid expansion ratios of 1.3 near the endwalls and 1.2 near the blade surfaces were used in these computations. To represent the vorticity accurately at inlet to the stator blade-row, a total of nine cells have been employed inside the end-wall boundary-layer thickness, which is of the order of 4% span.

III. Results and Discussion

The three-dimensional flowfield is discussed with the help of measurements at planes 1, 2, 3, which are located at 20% C_x downstream of stator, 60% C_x from rotor leading edge, and 20% C_x downstream of rotor, respectively. The transport of the stator viscous flow features within the rotor is also discussed in detail using smoke flow visualization. All of the measurements were carried out at the design condition.

A. Stator Exit

The stagnation pressure loss coefficient Y contours at plane 1 are shown in Fig. 2a. The high loss region in the middle of the plot is the stator wake. Figure 2a shows that 60% of the span is essentially two-dimensional flow. Most of the loss over the span is associated with the blade wake, but there is also additional loss near the hub and casing caused by the end-wall secondary flows. These loss cores can be identified at 10 and 85% of the blade span situated on the suction side of the passage. At the casing the loss core is more diffuse, and the maximum pressure loss is 28% less than the loss at the hub. The centers of the passage vortices are coincident with the maximum streamwise vorticity as shown in Fig. 2a. The centers of the passage vortices do not coincide with the locations of the maximum loss. They are located closer to the end walls than the maximum stagnation pressure loss position. The centers of high loss and streamwise vorticity will merge farther downstream. A local increase in loss can be seen at regions 1. This is caused by the interaction between the blade surface flows and the new end-wall surface flows at the suction surface corner.

At plane 1 the ensemble-mean velocities (not presented in the paper) indicate that the maximum amplitude of the periodic velocity fluctuation is less than 1% of the mean value. This is because the potential field of the rotor is relatively weak.

Contours of the time-mean phase-averaged turbulence intensity ($\overline{\langle\langle Tu_{\mathrm{rms}}\rangle\rangle}$) derived from three-axis hot-wire data are presented in Fig. 2b.

The mean turbulence intensity reaches a maximum value of 9% in the hub secondary flow, whereas it is 7% in the casing secondary flow. This indicates that the secondary flow at the hub is stronger than that at the casing. This is in keeping with the five-hole probe measurements. The center of the wake has a relatively high turbulence intensity of 6%. In the freestream region the turbulence intensity is very small (around 0.7%).

The mean turbulence-intensity data (Fig. 2b) present a similar picture to the stagnation pressure loss data (Fig. 2a). This indicates that the turbulence intensity is a good marker for identifying the flow structures.

B. Rotor Exit

Figure 3 summarizes the results of a relative frame five-hole probe traverse at plane 3. The data obtained from five equi-spaced radially disposed rotor leading edge Pitot tubes have been interpolated to provide a reference stagnation pressure for the traverse data at each radius.

Figure 3 presents the relative stagnation pressure losses as measured by the five-hole probe in the rotor. The high loss region near midspan is the wake. Figure 3 shows that at least 40% of the span (from 30–70%) is occupied by essentially two-dimensional flow. Near the hub, the loss associated with secondary flow is evident. A large hub passage vortex can be seen covering up to 25% of the span.

The loss associated with the tip leakage is centered at 95% span (Fig. 3). The loss core covers almost 55% of the passage width and 10% of the span. This plot suggests that the tip leakage flow is the dominant secondary flow at this location.

The time mean results presented in Fig. 3 have been carefully examined in conjunction with the yaw and pitch angles, axial velocity, and secondary velocity vector plots (not presented in this paper). The loss core (Fig. 3, region 1) is caused by a vortical structure rotating in the direction opposite to that of the leakage vortex. This structure can be caused either by the interaction between the stator and rotor casing secondary flow or by the rotor secondary flow. This is discussed further in Sec. III.D using the unsteady data.

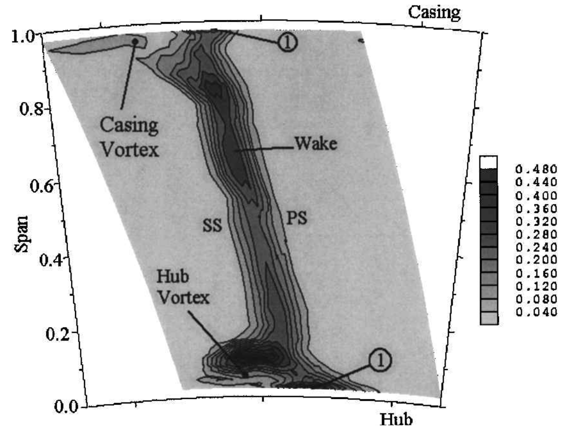

a) Y

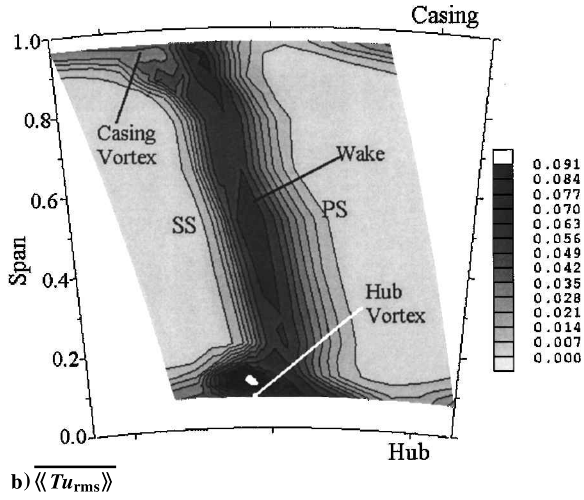

b) $\overline{\langle\langle Tu_{\mathrm{rms}}\rangle\rangle}$

Fig. 2 Stagnation pressure loss and time mean turbulence intensity at stator exit plane 1.

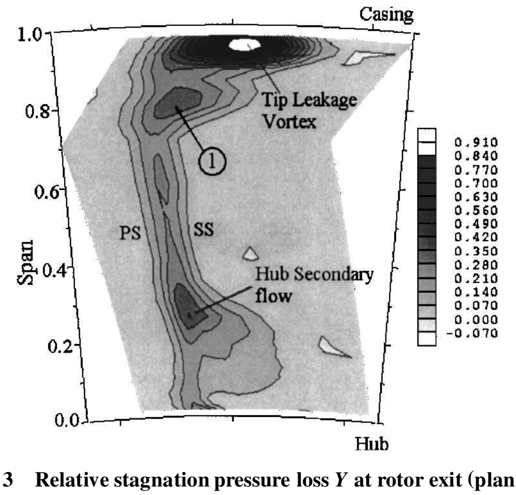

Fig. 3 Relative stagnation pressure loss Y at rotor exit (plane 3).

C. Smoke Flow Visualization of Rotor-Stator Interaction

Smoke flow visualization was carried out to identify the transport mechanisms of the stator wake and secondary flow features through the rotor blade row, at various spanwise locations. In the present paper the results from two particular experiments are reported. First, smoke was introduced through the stator trailing edge at midspan position to investigate the wake transport in the rotor passage. In the second experiment smoke was introduced in the stator hub region in order to study the stator passage vortex transport through the rotor. Photographs were obtained using a stroboscope while holding the camera shutter open to obtain a total of eight superimposed exposures.

Results from the first experiment are shown in Fig. 4 in the form of a sequence of smoke flow visualization pictures separated by equal intervals in time. The wake is identified with a white region in the middle of the passage. Fig. 4a shows the wake just inside the blade-row. The bowing of the wake is observed in Fig. 4a. As the wake is drawn into the rotor passage, it is convected at the local freestream velocity. The bowing of the wake is caused by the higher convection rate in the midpassage flow compared to the blade surface flows.

By the time $t/\tau = 0.286$ (Fig. 4b), the wake has been convected to 50% of the surface length on the suction side. The reorientation or shearing of the wake can be seen in this figure. The shearing of the wake occurs because the fluid close to the suction surface convects at a much higher rate than the fluid near the pressure surface. This leads to wake stretching on the pressure side leg of the wake (region 1). The wake centerline distortion and reorientation continues at $t/\tau = 0.571$ (Fig. 4c). By the time $t/\tau = 0.857$ (Fig. 4d), the wake has been convected to the rotor trailing edge. The net result of the bowing, the stretching, the shearing, and the distortion is that the wake appears to be concentrated on the suction surface at the rotor exit with a 'tail' stretching back to the rotor leading edge.[13,14] The same stator wake can be seen entering the adjoining rotor passage at time $t/\tau = 0.857$ (region 2).

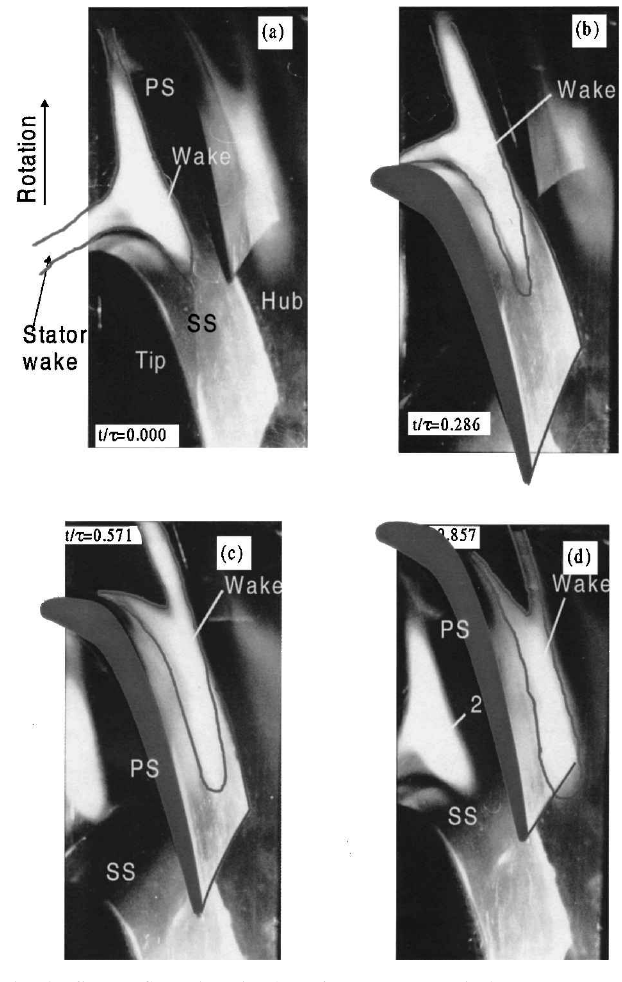

Fig. 4 Smoke flow visualization of stator wake within rotor passage at midspan in blade-blade plane: a) $t/\tau = 0.000$, b) $t/\tau = 0.286$, c) $t/\tau = 0.571$, and d) $t/\tau = 0.857$.

Results from the second experiment are shown in Fig. 5 as a sequence of smoke flow visualization pictures at four equal intervals in time, over one wake-passing period. The pictures were taken at the rotor exit looking upstream and perpendicular to the throat. Each picture shows the flow in three rotor passages at any instant in time, designated as passages 1, 2, and 3 respectively. In these pictures the stator passage vortex is identified with the white regions.

In passage 3 (Fig. 5a, $t/\tau = 0.000$), the smoke appears on the suction surface inside the blade passage. The smoke structure is circular in nature and confined to the rotor hub region on the suction surface.

In passage 2 (Fig. 5a) the smoke traces entered into the blade passage at an earlier instant in time and can now be observed in the throat region. The smoke structure in this passage consists of two regions. One is circular in nature near the rotor hub, and the other is elongated in the radial direction above the circular region. The smoke in the elongated region appears to be thinner.

The smoke structure in passage 1 (Fig. 5a) has some similarity with the smoke structure in passage 2. The smoke traces appear downstream of the rotor trailing edge. The smoke pattern in this passage is thinner than in the preceding passages indicating smoke dispersion caused by increased dissipation in the secondary flow.

Figure 5b occurs approximately after one-quarter of a rotor passing period ($t/\tau = 0.286$). Since the preceding time instant, the smoke traces in passage 3 have moved further downstream compared to Fig. 5a. The smoke trace in passage 2 has convected further downstream to the rotor trailing edge. The radial extent of the smoke has increased. Smoke from passage 1 has moved downstream appearing even more dispersed.

Figures 5c and 5d show the progression of the incoming secondary flow features through the blade passages at subsequent time instants. At time $t/\tau = 0.571$ (Fig. 5c) the smoke trace at the exit of passage 1 has almost disappeared, as the secondary flow features move downstream. At $t/\tau = 0.857$(Fig. 5d) smoke can be seen entering a new rotor passage designated as passage 4.

In general, it is observed that the secondary flow vortices are convected through the downstream blade row in a similar but not identical way to the wake. Because of the effects of vortex distortion, stretching, shearing, and varying convection rates, the vertically moving fluid appears to be concentrated on the suction side. A detailed description of the kinematic behavior of the passage vortices is presented in the following section.

D. Simple Vortex Transport Model

A comprehensive picture of wake-blade and vortex-blade interactions in the downstream blade row can be assembled from the flow visualization and unsteady measurements and simulations (presented later in this paper). A simple model for the stator passage vortex transport through the rotor is discussed with the help of a schematic presented in Fig. 6. The stator wake transport through the rotor blade row is also depicted at midspan.

The stator hub passage vortex is chopped by the downstream blade row in a similar way to the wake. It is then convected through the rotor passage at about the freestream velocity. The variation in transport velocity across the passage is responsible for the distortion of the vortex centerline as shown in Fig. 6. The bowed vortex tube appears to have two counter-rotating legs extending back to the leading edges of the adjacent blades. These are termed as the suction side leg (region 3, Fig. 6) and pressure side leg (region 2, Fig. 6) in the present context.

Reorientation or shearing of the vortex occurs because a fluid particle will convect along the suction surface at a much higher rate than a particle near the pressure surface. As the suction side leg of the vortex is accelerated away from the rear part, which remains in the vicinity of the leading edge, it stretches along the suction surface. The pressure side leg of the vortex stretches across the

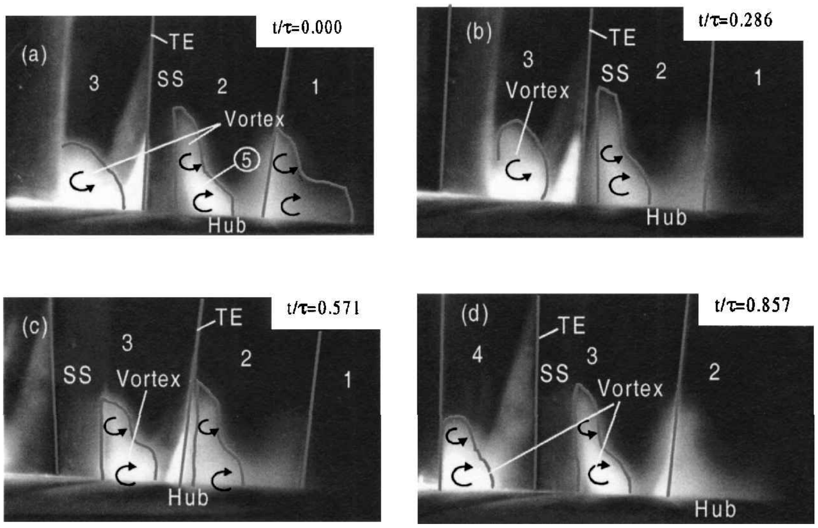

Fig. 5 Smoke flow visualization of stator vortex within rotor at hub in quasi-orthogonal plane: a) t/τ = 0.000, b) t/τ = 0.286, c) t/τ = 0.571, and d) t/τ = 0.857.

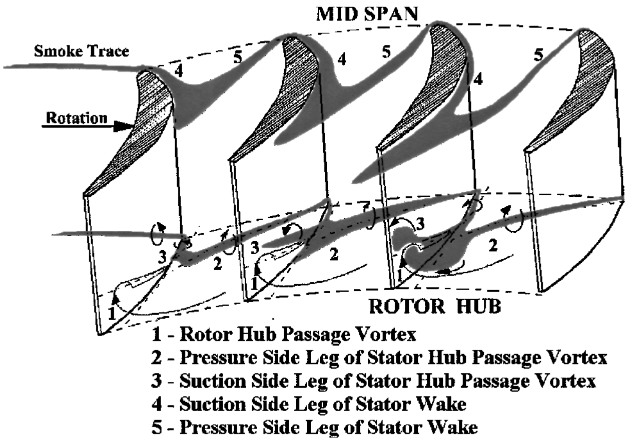

Fig. 6 Simple blade-vortex transport model.

passage. The stretching of the vortex tube results in the reduction of the vortex diameter with a concurrent increase in its angular velocity and subsequent increase in the dissipation rate.

Because of the flow modifications (distortion, stretching, and shearing), the stator hub vortex appears to be concentrated on the suction side with a tail extending up to the rotor leading edge on the pressure side of the passage.

The presence of the rotor passage vortices affects the transport of the stator passage vortices in the rotor. The kinematic interaction between the stator and the rotor passage vortices has two effects. First, the suction side leg of the stator passage vortex is displaced radially upwards over the developing rotor hub passage vortex. The pressure side leg of the stator passage vortex is counter-rotating to the rotor hub passage vortex. Additionally, the pressure side leg of the stator passage vortex, rotating in the same direction as the rotor passage vortex, is engulfed by the rotor passage vortex.

Similar phenomena are observed at the rotor tip, where the tip leakage and passage vortex interaction causes the stator features to move toward the midspan on the suction surface. These results are not shown in this paper for the sake of brevity.

E. Stator Wake and Vortex Transport

The turbulence intensity, obtained from three-axis hot-wire measurements, was used in tracking the stator flow inside the rotor. To extract the unsteadiness of the flow, the minimum level of the turbulence energy at each traverse point has been subtracted from the rms value. The result is given as

$$\langle\langle Tu_{\mathrm{aru}}\rangle\rangle = \sqrt{\langle\langle Tu_{\mathrm{rms}}\rangle\rangle^2 - \langle\langle Tu_{\mathrm{min}}\rangle\rangle^2} \tag{5}$$

This assumes that the minimum background turbulence intensity corresponds to the flow that would occur if the rotor inflow were steady. Figure 7 shows the contours of the additional random unsteadiness ($\langle\langle Tu_{\mathrm{aru}}\rangle\rangle$) at plane 2 over one wake passing period. Because of geometrical constraints, the traverse does not cover the full pitch.

A detailed description of the flowfield at plane 2 was reported by Hodson et al.[15] Only the stator viscous-flow transport will be described in this paper. Figure 7a shows that the midspan area of the suction surface is exposed to a low level of additional random unsteadiness. The remnants of a previous wake (region 2) can be seen near the pressure surface. Near the casing (region 1) the viscous flow originating from the casing in the stator row is beginning to appear at 85% span. At stator exit the same secondary flow can be observed at 90% span. Smoke flow visualization experiments and computational simulations that track particles through the flowfield suggest that the movement of the stator secondary flow toward the midspan is caused by the influence of the rotor tip leakage flow. As a result, the stator secondary flow is displaced toward the midspan.

Figure 7b occurs at one-quarter of a stator passing period after Fig. 7a. Now the suction surface is exposed to the incoming wake (region 4). The minimum levels of turbulence intensity at this plane are very small (less than 0.5%) in the freestream region (not shown in this paper). This indicates that regions of low turbulence intensity separate the stator exit perturbations as they pass through the rotor blades. Figure 7b also indicates that the contours reach a maximum value of 2.3% in the stator wake. The maximum turbulence level ($\langle\langle Tu_{\mathrm{rms}}\rangle\rangle$) in the stator wake at this plane is 3.8%. This value is lower than that at the stator exit (6.0%) indicating a decrease in turbulent kinetic energy of the stator wake. Other than the wake and stator casing secondary flow, a feature that is identified with the stator hub secondary flow is also present in Fig. 7b (region 3). This is at a higher radius (20% span) than indicated by the stator exit traverse (10% span). Numerical simulations and flow visualization show that this radial shift is caused by the effects of the influence of the secondary flow at the rotor hub, as discussed in Secs. III.C and III.D.

At $t/\tau = 0.625$ the wake (region 4) now extends over the full span. The stator casing secondary flow is just beginning to disappear in the plot, whereas the hub secondary flow is still present. The final plot (Fig. 7d) shows that the stator hub secondary flow now appears nearer the pressure surface at a lower radius. This is entirely consistent with the reduced effects of the rotor secondary flow near the pressure side of the passage.

The differing convection rates on the pressure and suction surfaces means that the transport of fluid that lies near the suction

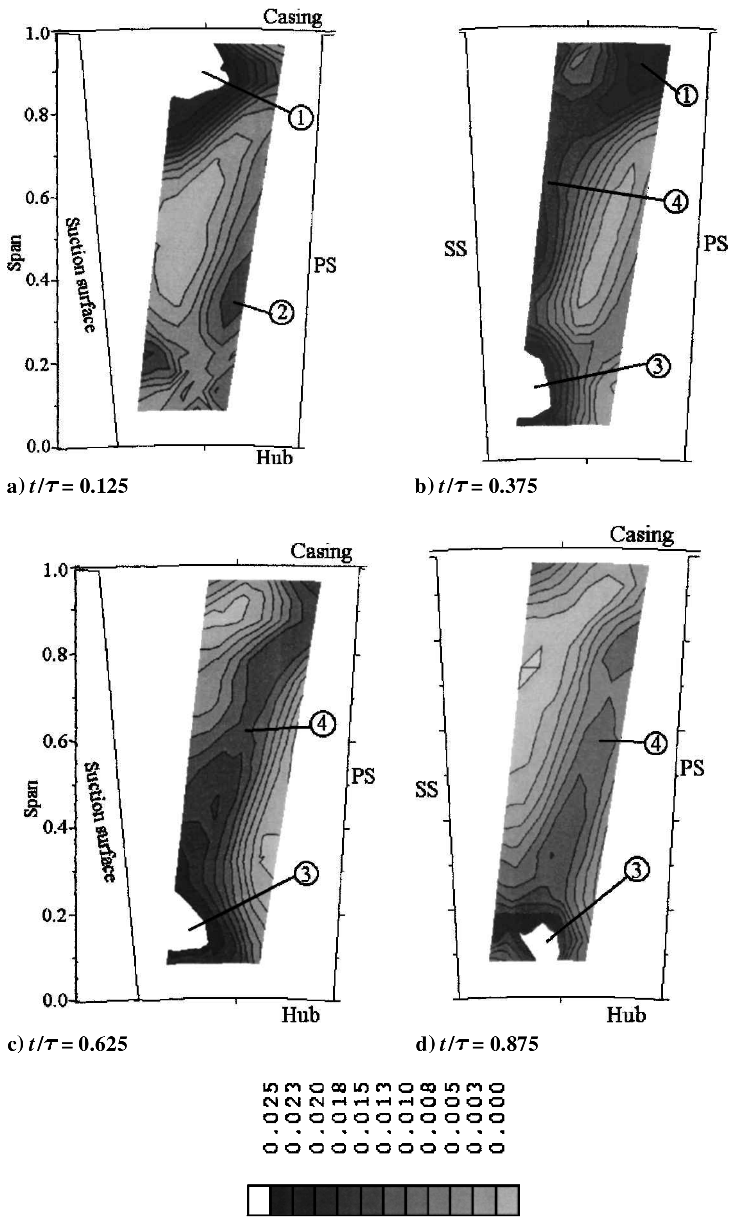

a) $t/T = 0.125$

b) $t/T = 0.375$

c) $t/T = 0.625$

d) $t/T = 0.875$

Fig. 7 Instantaneous $\langle\langle Tu_{\mathrm{aru}}\rangle\rangle$ near rotor midchord position (plane 2).

surface is much more rapid than that which lies close to the pressure surface. Because the traverse plane is located near midchord, most of the distortion that this difference causes would have already taken place. Consequently, the stator wakes and secondary flow features are expected to appear first at the traverse plane, nearer the suction side of the passage. This is illustrated by the data presented in Fig. 7.

The hot-wire measurements at plane 2 reveal that in the case of the stator secondary flows significant dissipation of the turbulence has occurred between the stator exit plane (9.1% maximum at hub) and the rotor midchord plane (3.8% maximum at hub). The maximum turbulence levels are much less at the rotor midchord position compared to the stator exit levels. This strongly implies that there is no turbulence generation caused by vortex cutting in this particular turbine. The reduction in turbulence levels occurs because of vortex stretching between the stator exit and rotor midchord position.

Figure 8 presents the contours of the parameter $\langle\langle Tu_{\mathrm{aru}}\rangle\rangle$ at four positions of the rotor blades, equi-spaced in time, over one stator passing period, at traverse plane 3. At time $t/\tau = 0.125$ the additional random unsteadiness is low throughout the passage (0.5%) except in the rotor wake (region 1) and secondary flow (regions 2 and 3). At this time, the increased levels of additional random unsteadiness are beginning to appear near the casing (to the right of region 2) and the hub (outwards of region 3). Figure 8b occurs one-quarter of a stator passage period after Fig. 8a. The unsteadiness has reached a maximum level of 6.5% to the right of the rotor trailing edge separated by a low turbulence region. Regions 4 and 5 are the stator casing and hub secondary flow vortices, respectively. Region 6 corresponds to the stator wake. The interaction between the stator flow and the rotor secondary flow is observed near the suction side of the blade, at around 25 and 70% of the blade span. It is also observed that region 5 is radially outward of region 3, indicating the radial movement of the stator flow features. By time $t/\tau = 0.625$ in Fig. 8c, the stator flow features (region 8) appear right on the suction side with a very high additional random unsteadiness of more than 6.5%, at the hub. Near the casing the rotor flow structure is more fragmented (region 7). This is caused by the interaction of the rotor leakage and passage vortices with the stator wake and passage vortices. At time $t/\tau = 0.875$ the flow is slowly reverting to the values at $t/\tau = 0.125$ with the maximum turbulence levels of the stator features reducing (regions 9 and 10) and the freestream fluid returning to low turbulence values.

In Figs. 7 and 8 the minimum turbulence intensities were subtracted out from the total values. Therefore, if the rotor features are

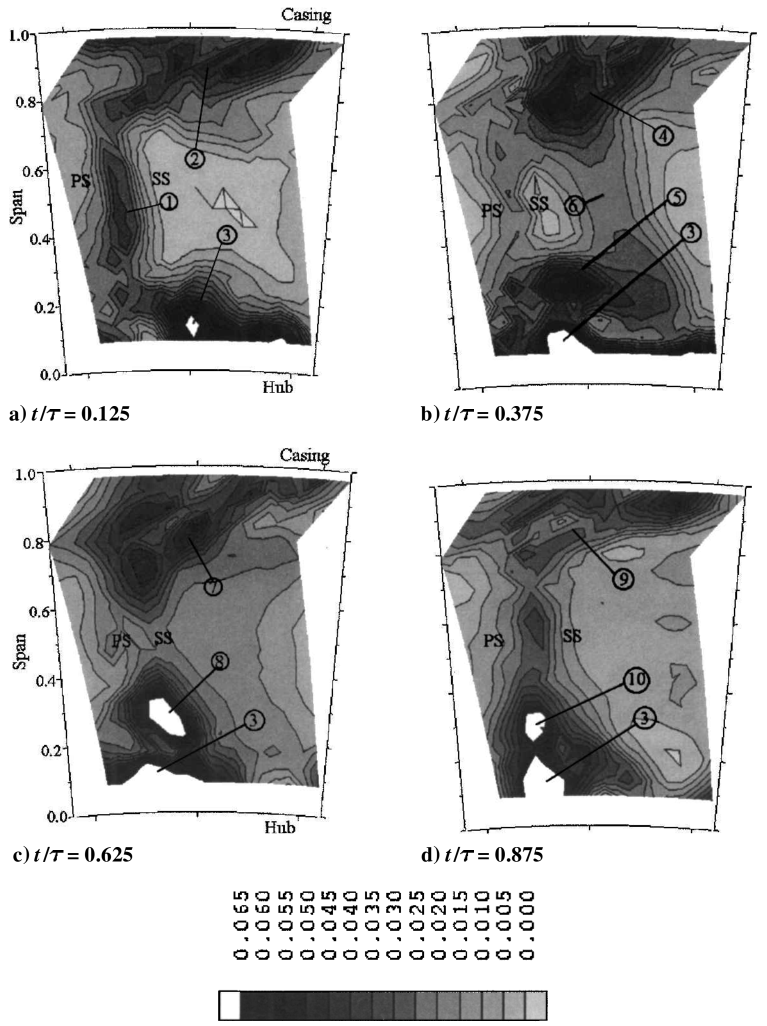

a) $t/\tau = 0.125$ b) $t/\tau = 0.375$

c) $t/\tau = 0.625$ d) $t/\tau = 0.875$

Fig. 8 Instantaneous $\langle\langle Tu_{\mathrm{aru}}\rangle\rangle$ at rotor exit (plane 3).

still observed in these plots, they have to be caused by the unsteadiness in the rotor wakes and secondary flows. This unsteadiness is caused by the presence of the stator flow inside the rotor. These stator flow features influence the development of the rotor surface boundary layers and in turn influence the rotor secondary flow. By affecting the laminar-turbulent transition of the blade surface boundary layers, the rotor profile loss is also affected.

By observing region 3 at all of the time instants, it can be seen that the rotor hub secondary flow moves radially and circumferentially, varying in size in one stator-passing period.

Because the measurement grid resolution of the five-hole probe data is better than the hot-wire data, the five-hole probe results were used here to describe the flowfield. Nevertheless, a very good agreement between the time average unsteady measurements and time steady five-hole probe data was observed. The unsteady features of the flow are discussed with the help of hot-wire data (Fig. 10). Figure 9 presents the secondary velocity vectors at the traverse plane 3 from the five-hole probe measurements. The secondary velocity vector is defined as the difference between the local velocity vector and a reference flow direction, which is 74 deg in this particular case. This angle is chosen because it coincides with the mean flow angle of the rotor hub and leakage vortices so that they become readily apparent. Various secondary flow features can be identified in this figure. At 20 and 90% blade span on the suction side of the passage (A & B), two clockwise-rotating vortices are observed. These are the rotor hub passage vortex and the tip leakage vortex, respectively. In addition to these two vortices, a vortical structure rotating anticlockwise can be observed near region D. This is a time-mean manifestation of the unsteady interaction between the rotor and the stator casing secondary flow.

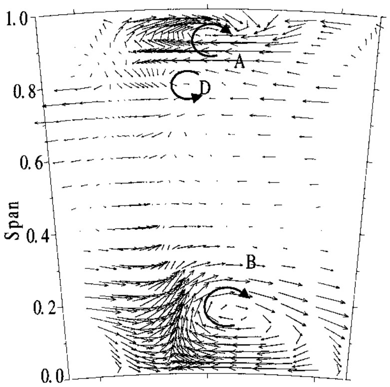

Fig. 9 Secondary velocity vectors at rotor exit plane 3 derived from five-hole probe data.

Figure 10 shows the time-varying secondary flowfield with the help of secondary velocity vectors, derived from hot-wire data. The unsteady secondary velocity vector is defined in the same way as in the steady case. At 20 and 90% blade span on the suction side of the passage (B & A), two clockwise-rotating vortices can be seen at all of the time instants. These are identified as rotor hub passage vortex and tip leakage vortex, respectively. At time $t/\tau = 0.125$ and $t/\tau = 0.375$ a counter-rotating vortex is observed just on the side of the rotor hub passage vortex (region C), which is because of the stator hub passage vortex. A close observation of the flow near the suction surface corner at time $t/\tau = 0.625$ reveals the presence of a vortex (region D). This vortex is just below the rotor tip leakage

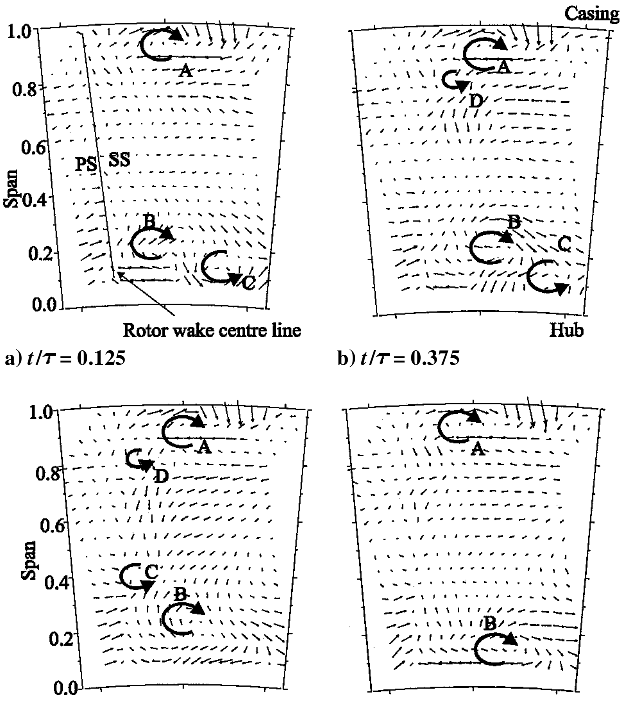

a) $t/\tau = 0.125$ b) $t/\tau = 0.375$

c) $t/\tau = 0.625$ d) $t/\tau = 0.875$

Fig. 10 Secondary velocity vectors at rotor exit (plane 3) derived from hot-wire data.

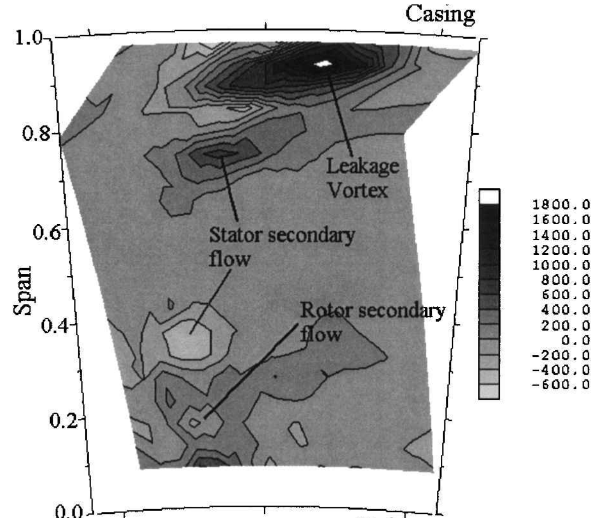

Fig. 11 Instantaneous axial vorticity at rotor exit (plane 3, $t/\tau = 0.625$).

vortex at 80% blade span, rotating in the opposite direction to the leakage vortex. As this is not always present, the result is probably caused by the interaction between the rotor and stator secondary flow. The varying strength of tip leakage flow can be observed at all the time instants, which is caused by the interaction of the suction side leg of the stator casing passage vortex with the leakage vortex, that is rotating in the same direction.

The contours of axial vorticity at plane 3 are shown in Fig. 11 at time $t/\tau = 0.625$. The velocity gradients in the r and θ directions can only be calculated from the measured data at a given traverse plane. Hence, only the axial component of the vorticity is presented here. The axial vorticity is given by

$$\zeta_x = \frac{1}{r}\left[\frac{\partial(rV_\theta)}{\partial r} - \frac{\partial V_r}{\partial \theta}\right] \tag{6}$$

The positive values of ζ_x indicate clockwise motion. The leakage vortex is confined to 15% of the span from the casing on the blade suction side. A region of negative vorticity can be observed just below the leakage vortex at 80% span. This corresponds to the interaction between the rotor and stator casing passage vortex. Another region of positive vorticity can also be observed below this secondary passage vortex at 75% blade span. This can be attributed to the stator passage vortex. At the hub, a region of positive vorticity can be observed near 22% span corresponding to the rotor hub passage vortex. The negative vorticity corresponding to the stator hub secondary flow can be observed above the rotor secondary flow region at 30% span.

IV. Comparison of Steady and Unsteady Simulations

Unsteady and steady Navier–Stokes simulations of the stage were carried out using the solvers described in Sec. II.D. Identical grids, numerical schemes, mixing length parameters, relaxation parameters, and boundary conditions were used for the steady and unsteady numerical simulations carried out in this paper. In unsteady simulations the upstream viscous features pass through the downstream blade row. To reduce the computation time and data storage, the unsteady simulations were carried out with 42 stator blades and 42 rotor blades. For a better comparison, the steady calculations were also carried out with each 42 stator and rotor blades. The small variation in stator solidity has only a small effect on the rotor flowfield. It has been shown later in the section that the measurements compare well with the unsteady simulations confirming the validity of the preceding assumption.

Figure 12a presents the contours of stagnation pressure loss coefficient Y from five-hole probe measurements and Fig. 12b from unsteady numerical simulations at the exit of the rotor (plane 3). The relative stagnation pressure values at the rotor leading edge were averaged in the pitchwise direction. These values were used in evaluating the relative stagnation pressure loss at rotor exit, assuming cylindrical stream surfaces. The general flow structure agrees well with the measurements both qualitatively and quantitatively. The leakage vortex (region 1) is dominant at this location. The loss core corresponding to the rotor hub secondary flow (region 2) can be observed at 25% blade span. The flow structure appearing at 80% blade span (region 3) is caused by stator-rotor interaction. Steady simulations do not accurately predict this feature's strength and location. Overall, there is good agreement between the measurements and the unsteady simulations. This increases the confidence in the numerical simulations and the conclusions that can be drawn from them.

The use of pitchwise averaging in a three-dimensional flow such as in this turbine destroys much of the flow detail. Any radial displacement of the flow feature will significantly change the pitchwise-averaged profile. However, because a downstream blade row will usually be designed to accept the pitchwise-averaged flow from an upstream blade row, it is instructive to compare the results in this way, in order that any limitations may be noted.

Figure 13 shows the spanwise distributions of the pitchwise-averaged rotor exit relative yaw angle, the envelope of its variation from the mean, and the stagnation pressure loss coefficient.

Results from the measurements, the steady and the unsteady numerical simulations are compared in Fig. 13. The familiar features of the secondary flow with overturning near the end wall and underturning toward the midspan can be seen in the relative yaw angle variations at the hub (Fig. 13a). Near the casing the flow is underturned as a result of the leakage vortex. A small underturning followed by overturning can be observed at 80% span, which is caused by the stator-rotor interaction as explained in Fig. 12. Accordingly, the steady simulation does not predict this flow feature.

At blade heights corresponding to the strongest stator secondary flow presence, differences between the steady and the unsteady computations become maximum (5-deg). The maximum difference between the steady and unsteady predictions of absolute flow angle is of the order of 10 deg at rotor exit corresponding to 25 and 80% span. This illustrates the limitations of steady flow calculations.

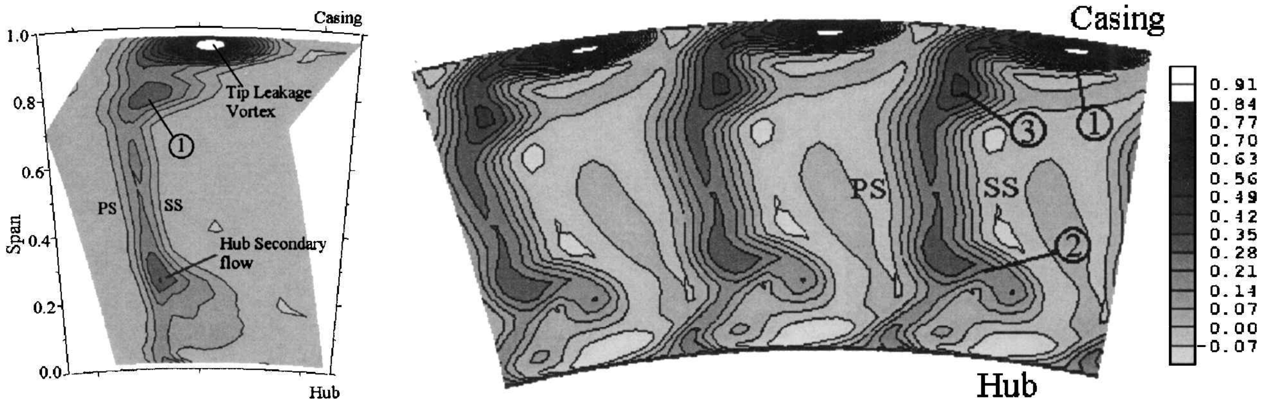

a) From measurements b) From unsteady simulations (three pitches)

Fig. 12 Relative stagnation pressure loss Y at rotor exit.

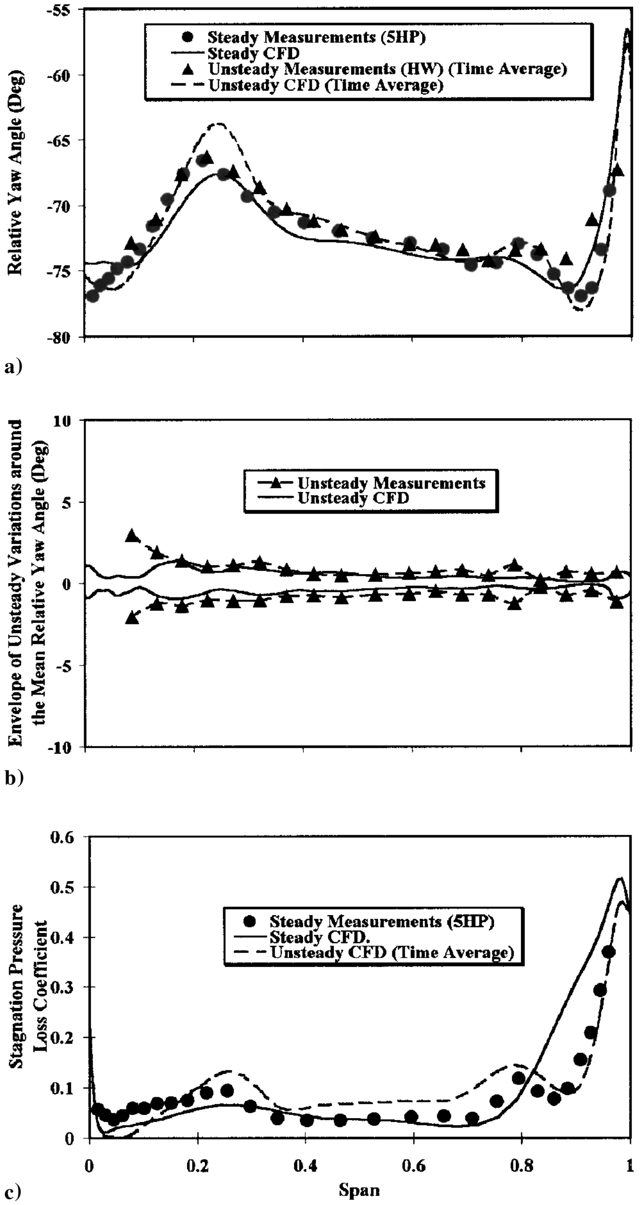

Fig. 13 Pitchwise-averaged spanwise distributions at rotor exit (plane 3): a) relative yaw angle, b) envelope of unsteady variation around the mean relative yaw angle, and c) Y.

The time-average unsteady hot-wire data are in good agreement with the steady five-hole probe data except near the tip region. This is because the hot-wire measurement accuracy is compromised in this region because of the relatively large gradients in yaw angle and random unsteadiness. Furthermore, the unsteady computations are in good agreement with the measured data.

Figure 13a also shows that there is no underturning at the end walls and overturning towards the midspan for this particular turbine (unlike that of Sharma et al.[2]).

Figure 13b shows the envelope of the phase-averaged variations around the mean relative yaw angle. The level of unsteadiness over most of the blade span is in agreement with measured unsteady data except near the hub. The amplitude of fluctuation is much less than the difference between steady and unsteady computations indicating that the nonlinear effects are caused by the vortex transport rather than simple periodic fluctuations.

Figure 13c shows the comparison of stagnation pressure loss coefficient between measurements and steady and unsteady computations. In calculating the relative stagnation pressure loss coefficient, it is assumed that the stream surfaces are cylindrical. There is a reasonable agreement between the five-hole probe measurements and the time-averaged unsteady computations. The steady computation is not able to predict the losses accurately near the rotor secondary flow regions and tip leakage flow.

V. Unsteady Loss

The predicted flowfield was interrogated from the perspective of loss production to determine the contribution of the unsteady flow to the time-averaged performance of the stage. The only accurate measure of loss in an unsteady flow is entropy.[16] All of the entropy produced within the flowfield will eventually pass through the exit boundary of the stage and be perceived as the stage loss. The unsteady loss can be defined as the difference between the average entropy flux passing through the exit boundary, in one wake-passing cycle, of an unsteady calculation and the corresponding entropy flux from a mixing-plane steady calculation. This is given as

$$\omega_u = \frac{1}{\tau}\left\{\int_0^\tau\int_0^P\int_0^r 2\pi r(\rho V_x s)\,\mathrm{d}r\,\mathrm{d}y\,\mathrm{d}t\right\}_u - \left\{\int_0^P\int_0^r 2\pi r(\rho V_x s)\,\mathrm{d}r\,\mathrm{d}y\right\}_s \tag{7}$$

The difference between the integrated entropy fluxes from steady and unsteady computations were used in evaluating the contribution of unsteady loss to the stage efficiency. This is given as

$$\Delta\eta = \left(\frac{\dot m\Delta h_0}{\dot m\Delta h_0 + T\omega}\right)_s - \left(\frac{\dot m\Delta h_0}{\dot m\Delta h_0 + T\omega}\right)_u \tag{8}$$

The contribution of the unsteady flow to the stage loss is about 3.2 percentage points of stage efficiency. This additional unsteady loss is about $\frac{1}{3}$ of the steady loss. The stage efficiencies calculated from steady and unsteady computations were 89.8 and 86.6%, respectively. The efficiency measured for this stage is 88.3% with an uncertainty of 0.8%. The measured and predicted efficiency values agree reasonably well. Although the unsteady loss seems relatively high, additional loss includes contributions from other steady phenomena. For example, when the wake passes through the downstream blade row, the flow incidence to the blade row changes temporally. Additional loss will be generated as a result of this effect, though it is small in this high-pressure turbine. In the mixing plane steady calculations the wakes and passage vortices are instantaneously mixed out at the exit boundary of the blade row. Conversely, in unsteady simulations these viscous structures are transported through the downstream blade row, generating additional losses caused by wake mixing and vortex stretching. It may not be possible to demonstrate that this difference in efficiencies predicted between the steady and unsteady simulations is less a result of the turbulence modeling and caused mainly by the unsteady conjecture. For example, insufficient mixing in the early part of the rotor passage would lead to higher loss value and vice versa. However, because the turbulence model is the same for both steady and unsteady simulations and a good agreement in the quantitative nature of the prediction in the steady flow condition, then it ought to be representative in unsteady flow conditions as well. In the turbine under investigation, unsteady measurements confirm that considerable vortex stretching has taken place. Hence, the main contribution to the unsteady loss is caused by wake mixing and vortex stretching in the downstream blade row.

VI. Conclusions

The development of steady and unsteady three-dimensional flow in a single-stage axial flow turbine has been described. The transport of viscous flow features within the rotor blade row has been analyzed.

In the case of the stator secondary flows, significant dissipation seems to occur as a result of vortex stretching, which takes place between the stator exit and the rotor midchord position.

It is observed that the stator secondary flow vortices are convected through the downstream blade row in a similar but not identical way to the wake. At the hub the kinematic interaction between the stator and the rotor passage vortices has two effects. First, the suction side leg of the stator passage vortex is displaced radially upward over the developing rotor hub passage vortex. Additionally, the pressure-side leg of the stator passage vortex is entrained into the rotor passage vortex. Similar phenomena were observed at the tip of the rotor blade row.

A simple model is proposed for the transport of the secondary flow vortices in the downstream blade row based on the understanding obtained from the measurements and the numerical simulations.

The time-averaged unsteady measurements are in good agreement with the steady measurements except near the tip region. Unsteady numerical simulations were found to be successful in predicting accurately the flow near the secondary flow interaction regions. Comparisons between the steady and the unsteady numerical simulations with measurements highlighted the need for unsteady computations.

The contribution of the unsteady flow to the stage loss has been evaluated using unsteady numerical simulations. The increase in loss between the steady and unsteady numerical simulations is thought to be caused by the stator wake mixing and passage vortex stretching in the downstream blade row, in the absence of a strong rotor potential field.

References

[1] Hodson, H. P., "Measurements of Wake Generated Unsteadiness in the Rotor Passages of Axial Flow Turbines," *Journal of Engineering for Gas Turbines and Power*, Vol. 107, No. 2, April 1985, pp. 467–476.

[2] Sharma, O. P., Renaud, E., Butler, T. L., Milsaps, K., Dring, R. P., and Joslyn, H. D., "Rotor-Stator Interaction in Multistage Axial Flow Turbines," AIAA Paper 88-3013, July 1988.

[3] Boletis, E., and Sieverding, C. H., "Experimental Study of the Three Dimensional Flow Field in a Turbine Stator Preceded by a Full Stage," *Journal of Turbomachinery*, Vol. 113, No. 1, 1991, p. 1.

[4] Walraevens, R. E., Gallus, H. E., Jung, A. R., Mayer, J. F., and Stetter, H., "Experimental and Computational Study of the Unsteady Flow in a 1.5 Stage Axial Turbine with Emphasis on the Secondary Flow in the Second Stator," American Society of Mechanical Engineers, Paper 98-GT-254, June 1998.

[5] Ristic, D., Lakshminarayana, B., and Chu, S., "Three-Dimensional Flow Field Downstream of an Axial-Flow Turbine Rotor," *Journal of Propulsion and Power*, Vol. 15, No. 2, 1999, pp. 334–344.

[6] Binder, A., "Turbulence Production Due to Secondary Vortex Cutting in a Turbine Rotor," *Journal of Engineering for Gas Turbines and Power*, Vol. 107, No. 4, 1985, pp. 1039–1046.

[7] Binder, A., Forster, W., Mach, K., and Rogge, H., "Unsteady Flow Interaction Caused by Stator Secondary Vortices in a Turbine Rotor," American Society of Mechanical Engineers, Paper 86-GT-302, June 1986.

[8] Sharma, O. P., Pickett, G. F., and Ni, R. H., "Assessment of Unsteady Flows in Turbines," American Society of Mechanical Engineers, Paper 90-GT-150, June 1990.

[9] Champagne, F. H., Schleicher, C. A., and Wehrmann, O. H., *Journal of Fluid Mechanics*, Vol. 28, 1967, p. 153.

[10] Denton, J. D., "The Use of a Distributed Body Force to Simulate Viscous Effects in 3D Flow Calculations," American Society of Mechanical Engineers, Paper 86-GT-144, June 1986.

[11] Denton, J. D., "The Calculation of Three Dimensional Viscous Flow Through Multistage Turbomachinery," American Society of Mechanical Engineers, Paper 90-GT-19, June 1990.

[12] Denton, J. D., "Multistage Turbomachinery Flow Calculation Program (MULTIP81)—User's Manual," Whittle Lab., Univ. of Cambridge, England, U.K., April 1997.

[13] Hodson, H. P., "An Inviscid Blade to Blade Prediction of a Wake Generated Unsteady Flow," *Journal of Engineering for GT & Power*, Vol. 107, No. 2, 1985, pp. 337–344.

[14] Hodson, H. P., "Blade Row Interactions in Low Pressure Turbines," *Blade Row Interference Effects in Axial Turbomachinery Stages*, VKI Lecture Series, 1998–02, von Karman Institute for Fluid Dynamics, Belgium, Feb. 1998, pp. 1–62.

[15] Hodson, H. P., Banieghbal, M. R., and Dailey, G. M., "3-Dimensional Interactions in the Rotor of an Axial Turbine," *Journal of Propulsion and Power*, Vol. 11, No. 2, 1995, pp. 196–204.

[16] Denton, J. D., "Loss Mechanisms in Turbomachines," American Society of Mechanical Engineers, Paper 93-GT-435, May 1993.